SAND80-1917
Unlimited Release
UC-25

Experimental Aspects of an Investigation of Macroscopic Ductile Failure Criteria

M. S. Soo Hoo, S. E. Benzley
and T. G. Priddy

Prepared by Sandia Laboratories, Albuquerque, New Mexico 87185 and Livermore, California 94550 for the United States Department of Energy under Contract DE-AC04-76DP00789.

Printed March 1981

Sandia National Laboratories

SF 2900-Q(3-80)

DISCLAIMER

Issued by Sandia Laboratories, operated for the United States Department of Energy by Sandia Corporation.

SF 1004-DF(11-77)

Printed in the United States of America
Available from
National Technical Information Service
U.S. Department of Commerce
5285 Port Royal Road
Springfield, VA 22161

NTIS price codes
Printed copy: $6.00
Microfiche copy: A01

PAGES 1 to 2

WERE INTENTIONALLY

LEFT BLANK

SAND80-1917
Unlimited Release
Printed March 1981

EXPERIMENTAL ASPECTS OF AN INVESTIGATION OF MACROSCOPIC DUCTILE FAILURE CRITERIA

M. S. Soo Hoo, 5835
S. E. Benzley, 5522
T. G. Priddy, 5522
Sandia National Laboratories
Albuquerque, New Mexico 87185

ABSTRACT

Experimental results for the ductile failure of 7075-T651 aluminum are presented in this report. Four separate shapes were tested to investigate the importance that macroscopic effective shear stress, hydrostatic stress, and plastic strain play in describing ductile failure of materials. The specimens used were: thin wall torsion tubes to create a state of pure shear, uniform hollow tubes to create a state of uniaxial stress; hour-glass shaped hollow tubes to create a state of biaxial stress; and notched round bars to create a state of triaxial stress.

Two proposed ductile failure criteria are discussed in conjunction with the experimental results presented. These results will be applied to the criteria in a later report.

1.0 Introduction

The ductile failure of metals can be characterized as a complex triaxial stress- and strain-dependent problem. The metallurgical mechanism that drives the ductile failure process is the initiation and coalescence of internal voids. One of the proposed ductile failure criteria [1, 2, 3] studied relates this microscopic void growth phenomenon to a macroscopic plastic failure strain in the presence of a triaxial stress field. The measure of triaxiality in this model is the ratio of hydrostatic stress to the von Mises or effective shear stress. For this model, failure is defined as that effective plastic strain level for which microvoids initiate and coalesce. This microscopic event does not necessarily coincide with the macroscopic event of fracture. (For this report, the term "failure" refers to a microscopic event and will be used in the context as defined by Hancock and MacKenzie. The term "fracture" refers to a macroscopic material separation.)

A second criterion under study is one proposed by Priddy [4, 5]. This criterion uses a cubic formulation for both yield and ultimate strength surfaces in three-dimensional stress space. The surfaces have a variable hydrostatic stress dependency feature and are not necessarily circular in deviatoric stress planes.

In order to quantitatively evaluate these failure criteria, experiments were performed on laboratory specimens configured to create various multi-axial stress fields. Four specimen shapes are used: 1) pure shear torsion; 2) uniaxial tubular; 3) biaxial tubular; and 4) triaxial notched round bars.

For quantification of these ductile failure criteria, three materials with varying degrees of ductility were considered. These materials were: 7075-T651 aluminum, a material with a modest amount of ductility; ASTM A-533 (grade B) steel and AISI 304 stainless steel, two reactor grade steels with significant amounts of ductility.

This report is confined to the experimental details of measuring the response of 7075-T651 aluminum for application to the proposed ductile failure criteria. The experimental results are also discussed and will be applied to the criteria in a later report [6].

2.0 Ductile Failure Criteria

The Hancock and MacKenzie [2] model under consideration is a macroscopic model based on the phenomena of microscopic void initiation and growth. This model relates effective plastic strain at failure, $\bar{\varepsilon}_p^f$, to a ratio of hydrostatic stress and effective shear stress. (The superscript "f" in $\bar{\varepsilon}_p^f$ refers to the effective plastic strain occurring at failure.) Equation 1 is the form of the Hancock and MacKenzie model.

$$\bar{\varepsilon}_p^f = \alpha \exp\left(-\frac{3}{2}\,\frac{\sigma_m}{\bar{\sigma}}\right) \tag{1}$$

$\bar{\varepsilon}_p^f \equiv$ effective plastic strain at failure

$$= \frac{\sqrt{3}}{2}\left[(\varepsilon_1 - \varepsilon_2)^2 + (\varepsilon_2 - \varepsilon_3)^2 + (\varepsilon_3 - \varepsilon_1)^2\right]$$

$\varepsilon_1, \varepsilon_2, \varepsilon_3 \equiv$ principal strain components

$\alpha \equiv$ material constant related to void kinematics

$\sigma_m \equiv$ mean or hydrostatic stress

$$= \frac{1}{3}\left(\sigma_1 + \sigma_2 + \sigma_3\right),\ \sigma_1, \sigma_2, \sigma_3 \text{ are principal stresses}$$

$\bar{\sigma}$ ≡ effective stress

$$= \frac{1}{\sqrt{2}} \left[\left(\sigma_1 - \sigma_2\right)^2 + \left(\sigma_2 - \sigma_3\right)^2 + \left(\sigma_3 - \sigma_1\right)^2 \right]^{\frac{1}{2}}$$

A graphical representation of Equation 1 is shown in Figure 1.

Hancock and MacKenzie define failure to occur at that strain level $\left(\bar{\varepsilon}_p^f\right)$ when microvoids initiate and coalesce. This failure does not necessarily coincide with fracture since it is possible for voids to initiate before the maximum load or fracture is achieved.

For a torsion test, the constant α is identically equal to the effective plastic strain $\bar{\varepsilon}_p^f$ at failure (i.e., when σ_m vanishes in pure shear).

The failure criterion given by Equation 2 originally proposed by Priddy [4] is phenomenological.

$$a\sum_{ij}\tau_{ij}^2 + b\sum_{i}\sigma_i^2 + c\sum_{ij}\sigma_i\sigma_j = 3d\sigma_m + 3e\sigma_m \cdot I_2 + f \cdot I_3 + 1 \qquad (2)$$

(a, b, c, d, e, f) ≡ material strength dependent constants

σ_i ≡ normal stress components $(\sigma_1, \sigma_2, \sigma_3)$

I_2 ≡ second stress invariant

I_3 ≡ third stress invariant

ij ≡ ordered pairs [(1,2), (2,3), (3,1)]

This model proposes combined yield and fracture strength surfaces, as shown in Figure 2. Reference 5 extends this model to include the effective plastic strain at failure.

This study uses both experimental and analytical techniques to quantify ductile failure criteria parameters. First, experiments are

arried out on specimens that produce uniaxial, pure shear, biaxial, and triaxial stress states. The uniaxial test: 1) provides an effective stress-strain law for use in subsequent finite element calculations, and 2) identifies a point of material failure produced by a uniaxial load history. Experiments performed on the pure shear, biaxial, and triaxial specimens generate load-displacement records that are used to establish failure limits under the various stress states.

Next, finite element models of each of the non-uniaxial specimens are analyzed using the effective stress-strain curve from the uniaxial specimen test. The finite element calculations are terminated at the fracture load level of the corresponding experiment.. The stress and strain state at the instant of specimen failure, determined metallurgically, is then obtained from the output of the finite element model.

Perhaps one of the more difficult experimental aspects of measuring ductile failure parameters is that of detecting failure as defined by Hancock and MacKenzie [2]. Generally, this definition of failure is difficult to apply since microscopic voids can initiate within samples long before final fracture has occurred. In order to apply this definition, one must load the initial sample to fracture, then load subsequent samples to various strains below the fracture strain of the initial, fractured sample. These subsequent samples are unloaded at the various strain levels and examined metallographically for indications of void initiation. The point of failure would then be defined as that stress and strain level at which void initiation was first detected.

For the aluminum material under consideration, this procedure of first loading, unloading, and then examining samples (for voids) at various strain levels was followed. The results of this study will be discussed in a later section.

Once the ductile failure criteria have been quantified, and the finite element codes have been shown to be able to predict the relevant stresses and strains, it is possible to locate the actual failure initiation site in a sample. The computer analysis can be used to predict the site on the specimen cross section which will undergo the critical stresses and strains necessary to cause failure according to one of the previously mentioned ductile failure criteria [2, 3, 4, 5]. The accuracy of this type of analysis can be verified by performing fractographic studies of fractured samples to determine failure initiation sites.

3.0 Material Condition

All specimens were fabricated from 38.1-mm 7075-T651 aluminum plate, according to Federal Specification QQ-A-250/12. The specimens were oriented so that the longitudinal axis of each specimen was perpendicular to the plate rolling direction (the long transverse direction).

4.0 Test Equipment

All specimens were tested with a closed-loop, electro-hydraulic test system. For the samples subjected to a tensile load, spherical ball joints were incorporated into the load chain to reduce bending stresses caused by misalignment. For compressively loaded samples, spherically-seated compression platens were used for applying the load. The axial load for the biaxial samples was applied by the hydraulic frame, and internal pressure was independently controlled.

All samples were loaded at a strain rate of approximately 10^{-4} sec^{-1} (biaxial samples were pressurized at .07 MPa/sec).

5.0 Multiaxial Stress State Specimens

With the proper selection of specimen shapes, it was possible to produce desired stress states in a particular material. Four specimen shapes were selected to provide different states of stress: 1) shear ($\sigma_1 = -\sigma_2$, $\sigma_3 = 0$); 2) uniaxial ($\sigma_2 = \sigma_3 = 0$); 3) biaxial ($\sigma_3 = 0$); and 4) triaxial. These specimens are called, respectively: torsion, uniaxial tensile, biaxial tensile, and triaxial notched round bars (Figures 3, 4, 5, 6). Table 1 summarizes the specimens and their associated values of principal stress.

A finite element computer code [7, 8] was used in the design of these specimen shapes. In particular, the triaxial design received the most detailed analysis since it was the most complex. For this type of specimen, the degree of hydrostatic stress can be varied by varying the notch root radius. Calculations were performed on the notched round bar geometry to select three radii which would produce hydrostatic stresses between 300 and 500 MPa.

Figure 7 shows a postulated failure envelope on the effective shear stress, hydrostatic stress plane [8]. The stress states at failure for all samples produce a locus of points which defines the envelope. For the torsion sample, the net mean stress vanishes. Because the uniaxial sample is a hollow tube design, the radial and tangential stresses (σ_2, σ_3) are assumed to be zero and not to contribute to the mean stress. The biaxial sample is essentially a

thin-walled pressurized tube and is stressed in the longitudinal and tangential direction. The radial stress is assumed to be zero. The axial load and internal pressure of the biaxial sample can be varied to control the relative magnitude of principal stresses. The axial, radial, and circumferential stresses of the notched round bar samples produce high mean stresses.

Figure 1 is a graphical representation of the Hancock-MacKenzie model. This postulated failure envelope is plotted on an axis of $\sigma_m/\bar{\sigma}$ vs $\bar{\varepsilon}_p^f$, plastic strain at failure, and is obtained from Equation 1. The torsion sample provides a point on the $\bar{\varepsilon}_p^f$ axis since the ratio $\sigma_m/\bar{\sigma}$ vanishes. The other samples, under different stress states at failure, provide different points along the failure envelope in Figure 1 and Figure 7.

5.1 Torsion Specimens

Figure 3 shows the torsion specimen design. The hollow, waisted geometry restricts fracture to the center section and also minimizes radial stresses. Prototype specimens were initially filled with a soft rubber to reduce the possibility of a premature fracture due to a geometric buckling instability. However, preliminary tests showed that the wall thickness was sufficient to preclude buckling. The rubber filler was not used in subsequent tests. Torque and angle of twist were the recorded parameters.

5.2 Uniaxial Specimens

Figure 4 illustrates the axisymmetric hollow specimen design used in order to reduce radial stresses and thus approximate a uniform uniaxial stress state.

Each specimen was instrumented with two axial strain gases to compensate for bending. A 25-mm extensometer was also used in measuring total axial displacements in the gage section.

5.3 Biaxial Specimens

To produce a two-dimensional stress state, specimens shown in Figure 5 were loaded axially and pressurized internally. In the testing of axially loaded, internally pressurized samples, the ratio of the longitudinal to transverse stress is an important parameter to control. Many biaxial tube experiments reported in the literature [9, 10] have been conducted with the samples subjected to a constant ratio of engineering stress. Because of experimental difficulties, a majority of biaxial testing is not performed where the sample is subjected to a constant ratio of true stress. (True stress ratio refers to the ratio of circumferential to longitudinal stress, based on instantaneous cross sectional area.) However, despite such difficulties, it is often necessary to maintain a constant true stress ratio to minimize the possibility of premature fracture as a result of geometric instability. Jones and Mellor [11] have performed a variety of biaxial experiments on thin-walled cylinders using constant true stress ratios. They propose that for samples subjected to a constant true stress ratio less than 1.0, rupture would occur by a fracture propagating circumferentially rather than longitudinally. This longitudinal fracture would be due to a geometric instability as opposed to the desired material instability.

For materials that do not exhibit a high degree of elongation, true stresses can be approximated by engineering stresses. This approximation is useful for the 7075-T651 aluminum under consideration. For ease of experimentation, the biaxial samples were loaded with a constant engineering stress ratio. However, in order to preclude fracture by geometric instabilities, a stress ratio of 1.0 was not exceeded. Also, as an aid to preclude premature fracture, the central gage section of the specimen was waisted to restrict failure to the center.

Biaxial testing was done with one electro-hydraulic test frame and two control consoles. The hydraulic actuator applied an axial load to the specimen. Also, the same hydraulic power supply was used to supply internal pressure to the specimen. Two independently controlled servo valves were used to control the axial load and internal pressure. Figure 8 is a block diagram of the instrumentation used in performing the series of biaxial tests. Instrumentation was set up to load the samples at constant stress ratios between .30 and .66.

Diametrical and axial displacements were measured by strain gage extensometers.

5.4 Triaxial Specimens

The notched round bar specimens were used to define points on the upper portion of the curve in Figure 1, for a mean-to-effective stress ratio between 1.0 and 2.0. These specimens also provided points for the right-hand portion of the envelope shown in Figure 7. Three root radii, .81 mm, 3.18 mm, and 6.35 mm, were selected to provide a variation in mean stress, in the region $1.0 < \frac{\sigma_m}{\bar{\sigma}} < 2.0$. Figure 6 illustrates the actual specimen geometry adopted.

Each specimen was instrumented with two diametrically opposed extensometers which were attached straddling the machined notch. The extensometers had an initial gage length of 12.7 mm. Also, a diametral extensometer was used to measure diametrical strain.

Reference 12 describes the use of these triaxial samples subjected to an axial compressive load rather than to the axial tensile load as described above. That work, done in conjunction with this particular study, reports on the observed hydrostatic-stress dependency of yield of 7075-T651 aluminum.

6.0 Experimental Results

Figures 9-15 show the experimental data collected for all four specimen types. As an indication of experimental scatter, the extreme curves for each type of test are plotted. For Figures 9, 10, and 15, each set of curves represents the results of five to seven samples. The curves for the biaxial specimens (Figures 11-14) represent three to five samples. A majority of the samples were loaded to fracture. Several were unloaded prior to fracture and saved for subsequent microscopic examination.

Localized necking was observed in all uniaxial specimens, with final fracture occurring within the gage section of the axial strain gages. The torsion samples failed circumferentially at the waist region.

Table 2 presents the initial and final dimensions of the fractured uniaxial samples. (For specimen 5, the test was stopped just prior to fracture. This specimen was subsequently sectioned and examined metallurgically for voids.) With these dimensions converted to plastic strains, the constant α can be computed from Equation 1. The plastic strains at fracture are presented in Table 3.

As mentioned above, the biaxial samples were loaded under a constant engineering stress ratio (as opposed to a constant true stress ratio). This ratio was varied from .30 to .66 as shown in Figures 11-14. Also, as mentioned above and in [11], this ratio was maintained below 1.0 (a case of balanced biaxial tension) to reduce the possibility of premature rupture due to a longitudinal fracture. Tested samples examined did rupture circumferentially.

The torsion and uniaxial samples exhibited very little data scatter. However, the triaxial samples exhibited data scatter which deserves some discussion. Considering Figure 15, the sharp notch data shows the greatest, and the mild notch data shows the least amount of variability. This differing amount of scatter is believed to be due to fixturing misalignment. Misalignment would cause bending stresses to exist within the notch region. With increasing notch severity, the material within a notch region behaves in a more brittle manner. Since brittle-behaving materials are more susceptible to bending stresses, it would be expected that the sharp notch sample would exhibit more data scatter. An effect of this misalignment can be seen in fractographs of fractured samples, which will be discussed later.

The mild notch sample behaves in a more ductile manner. This increased ability to flow plastically allows the specimen to realign itself and thus not be as susceptible to misalignment bending stresses.

7.0 Metallography and Fractography

As mentioned in previous sections, uniaxial and triaxial samples were loaded to various strain levels (prior to fracture), unloaded, and examined metallographically in the region of expected failure. For the triaxial tests, Figure 15 shows the maximum strain level

achieved before fracture. A comparison of the loading curves for both the fractured and unloaded samples revealed that the unloaded samples were loaded very close to fracture.

There were no detectable signs of void initiation in any of the samples. Since these samples examined for void initiation were so close to fracture and yet exhibited no signs of initiation, it is likely that voids did not form until just before the very instant of fracture. From this conclusion, failure appears to coincide with fracture (as specified above and in [2]). The appropriate quantities of stress and strain at failure can then be approximated based on the data at fracture.

By defining failure to occur at the same instant as fracture, one can conveniently use the final dimensions to compute effective plastic failure strains. In particular, the dimensions presented in Table 2 for fractured uniaxial samples can be employed in calculating plastic failure strains.

As mentioned in the previous section on "Ductile Failure Criteria," it is possible to predict the actual failure initiation site by using finite element codes in conjunction with the ductile failure criteria. This type of prediction can be verified experimentally by examining the profile of secondary cracking and the surface of primary cracking. The notched round bar samples were subjected to this type of examination.

Optical metallography was used to determine the approximate failure initiation site and the direction of crack propagation. Figure 16 shows sketches of the fracture profile and secondary crack branching that occurred for each of the three notch radii. These

cracks were typically .4 to .8 mm long and extended .1 to .8 mm below the primary fracture surface. Examination of various profiles showed the secondary cracks to be radial.

The approximate failure initiation site can be located by observing where the crack branching occurs and noting that the secondary cracks tend to form an acute angle to the direction in which the primary crack propagates. For the mild notch (6.35 mm root radius), secondary cracking occurs close to the center of the specimen cross section. These cracks show the primary crack to travel from the center of the sample. For the sharp notch sample, secondary cracking occurs close to the root of the notch. The crack branching for the sharp notch samples show that the primary crack travels from the notch root inward. Secondary cracking is somewhat ambiguous for the intermediate notch. These secondary cracks were observed to propagate both toward the notch root and toward the specimen center. This double phenomenon indicates that failure initiated at some location midway between the notch root and center.

Figure 17 shows scanning electron microscope fractographs for the three notch samples. These fractographs were taken perpendicular to the primary fracture surface. The elongated grain structure of the plate material made interpretation of the SEM fractographs difficult. However, some observations about the fracture surface can be made.

The SEM fractograph for the mild notch sample shows dimples at the center of the specimen. For a specimen with a sharp root radii, dimples are apparent in the vicinity of the machined notch, approximately .09 mm from the notch surface. The SEM fractograph of the intermediate notch sample reveals dimples near the center of the

sample cross section and also near the notch surface of the sample [13, 14].

8.0 Conclusion

A selection of samples was tested to generate data to be used later in quantifying criteria on ductile failure. In particular, the torsion sample provided failure data for material subjected to zero mean stresses. Stress-strain relationships were obtainable from hollow uniaxial samples. These relationships were used in numerically predicting the behavior of more complex specimen geometries.

The triaxial samples were perhaps the most useful of all samples. This notched round bar configuration is versatile in several ways: 1) depending on the manner of loading, either a hydrostatic tensile or a hydrostatic compressive stress field can be created; 2) varying degrees of hydrostatic stress can be achieved by merely varying the notch root radius; and 3) the axisymmetric geometry is relatively simple to analyze with finite element computer codes.

SEM fractography interpretation was difficult due to the elongated grain structure of the rolled plate material. However, SEM analysis provides evidence that failure began as microvoid coalesence around precipitates.

Optical metallography reveals secondary crack branching as seen in a profile view of the primary crack surface of the triaxial samples. The direction of propagation of these branches gives a qualitative indication of failure initiation site. These branches reveal that failure occurs: in the center of mildly notched samples, in the vicinity of the notch root of sharply notched samples, and in a

region midway between the center and the notch of intermediately notched samples.

Further metallographic examination of unloaded (but intact) samples exhibited no signs of microvoids or microcracks. This type of examination indicates that failure (defined by microvoid initiation and coalescence) occurs near the fracture load in the material. The appropriate stresses and strains at failure, then, can be approximated by the stresses and strains at fracture.

9.0 References

1. F. A. McClintock, "A Criterion for Ductile Fracture by Growth of Holes," J. Appl. Mech., pp. 363-371, June 1968.
2. J. W. Hancock and A. C. MacKenzie, "On the Mechanisms of Ductile Failure in High-Strength Steels Subjected to Multi-Axial Stress-States," J. Mech. Phys. Solids, Vol. 24, pp. 147-169, 1976.
3. A. C. MacKinzie, J. W. Hancock, and D. K. Brown, "On the Influence of State of Stress on Ductile Failure Initiation in High Strength Steels," Eng. Frac. Mech., Vol. 9, pp. 167-188, 1977.
4. T. G. Priddy, S. E. Benzley, and R. L. Johnson, "The Dual Characteristics of Yield and Ultimate Strengths as Applied to Two Grades of Beryllium," SAND77-0122, National Technical Information Service, Springfield, VA, February 1977.
5. T. G. Priddy, S. E. Benzley, and L. M. Ford, "A Consistent Stress-Strain Ductile Fracture Model as Applied to Two Grades of Beryllium," SAND79-2126, National Technical Information Service, Springfield, VA, January 1980.
6. S. E. Benzley, T. G. Priddy, and M. S. Soo Hoo, Unpublished research on the application of experimental-analytical data to ductile failure criteria.
7. S. E. Benzley, T. G. Priddy, and M. S. Soo Hoo, Unpublished research on the stress analysis of multi-axial experiments for the ductile fracture of 7075-T6 aluminum.
8. S. E. Benzley, T. G. Priddy, and J. P. Hickerson, "An Experimental-Analytical Comparison of the Ductile Failure of Notched Tensile Bars," SAND77-0727, National Technical Information Service, Springfield, VA, October 1977.
9. E. A. Davis, "Yielding and Fracture of Medium Carbon Steel Under Combined Stress," J. Appl. Mech., Vol 67, pp. A13-A24, 1945.
10. M. J. Hillier, "Tensile Plastic Instability of Thin Tubes-I," J. Mech. Sci., Vol. 7, pp. 531-538, 1965.
11. B. H. Jones and P. B. Mellor, "Plastic Flow and Instability Behavior of Thin-Walled Cylinders Subjected to Constant-Ratio Tensile Stress," J. Strain Analysis, Vol. 2 (1), pp. 62-72, 1967.
12. S. E. Benzley, T. G. Priddy, and M. S. Soo Hoo, "Hydrostatic Stress Dependent Yield of 7075-T6 Aluminum," SAND79-2220, National Technical Information Service, Springfield, VA, March 1980.
13. "Interpretation of Scanning-Electron-Microscope Fractographs," Metals Handbook-Fractography and Atlas of Fractographs, Vol. 9, p. 67, 1974.
14. J. T. Healey, Materials Characterization Department, Sandia National Laboratories, private communications.

10.0 Tables

	σ_1	σ_2	σ_3	σ_m	$\bar{\sigma}$
Torsion	$-\sigma_2$	$-\sigma_1$	0	0	$\sqrt{3}\sigma_1$
Uniaxial	σ_1	0	0	$\frac{1}{3}\sigma_1$	σ_1
Biaxial	σ_1	σ_2	0	$\frac{1}{3}(\sigma_1 + \sigma_2)$	*
Triaxial	σ_1	σ_2	σ_3	$\frac{1}{3}(\sigma_1+\sigma_2+\sigma_3)$	*

*follows the general form of $\bar{\sigma}$ defined in Equation 1

TABLE 1 - Selected Values of Principal Stress

Specimen Number	Original Outer Diameter (mm)	Final Outer Diameter (mm)	Original Wall Thickness (mm)	Final Wall Thickness (mm)
1	12.76	11.89	1.70	1.52
2	12.76	11.84	1.70	1.52
3	12.76	11.96	1.70	1.52
4	12.76	11.89	1.70	1.52
5	*	*	*	*
6	12.76	11.89	1.70	1.52
7	12.76	11.79	1.70	1.52

*Sample unloaded before fracture

TABLE 2 - Initial and Final Uniaxial Specimen Geometry

Specimen Number	Radial Fracture Strain	Tangential Fracture Strain
1	0.099	0.066
2	0.099	0.070
3	0.086	0.061
4	0.099	0.066
5	*	*
6	0.099	0.066
7	0.099	0.073

*Sample unloaded before fracture

TABLE 3 - True Plastic Strains at Fracture*

11.0 List of Figures

1. Hancock-MacKenzie model - $\frac{\sigma_m}{\bar{\sigma}}$ vs $\bar{\varepsilon}_p^f$
2. Cross-section of Priddy model taken perpendicular to hydrostatic axis
3. Torsion specimen drawing
4. Uniaxial specimen drawing
5. Biaxial specimen drawing
6. Triaxial specimen drawing
7. Predicted failure locus
8. Diagram for pressurization of biaxial specimens
9. Torsion data - load vs angle of twist
10. Uniaxial data - load vs displacement
11. Biaxial data - load, pressure vs axial elongation (.30)
12. Biaxial data - load, pressure vs axial elongation (.32)
13. Biaxial data - load, pressure vs axial elongation (.55)
14. Biaxial data - load, pressure vs axial elongation (.66)
15. Triaxial data - load vs displacement
16. Profile of secondary cracking
17. SEM fractographs of primary cracking

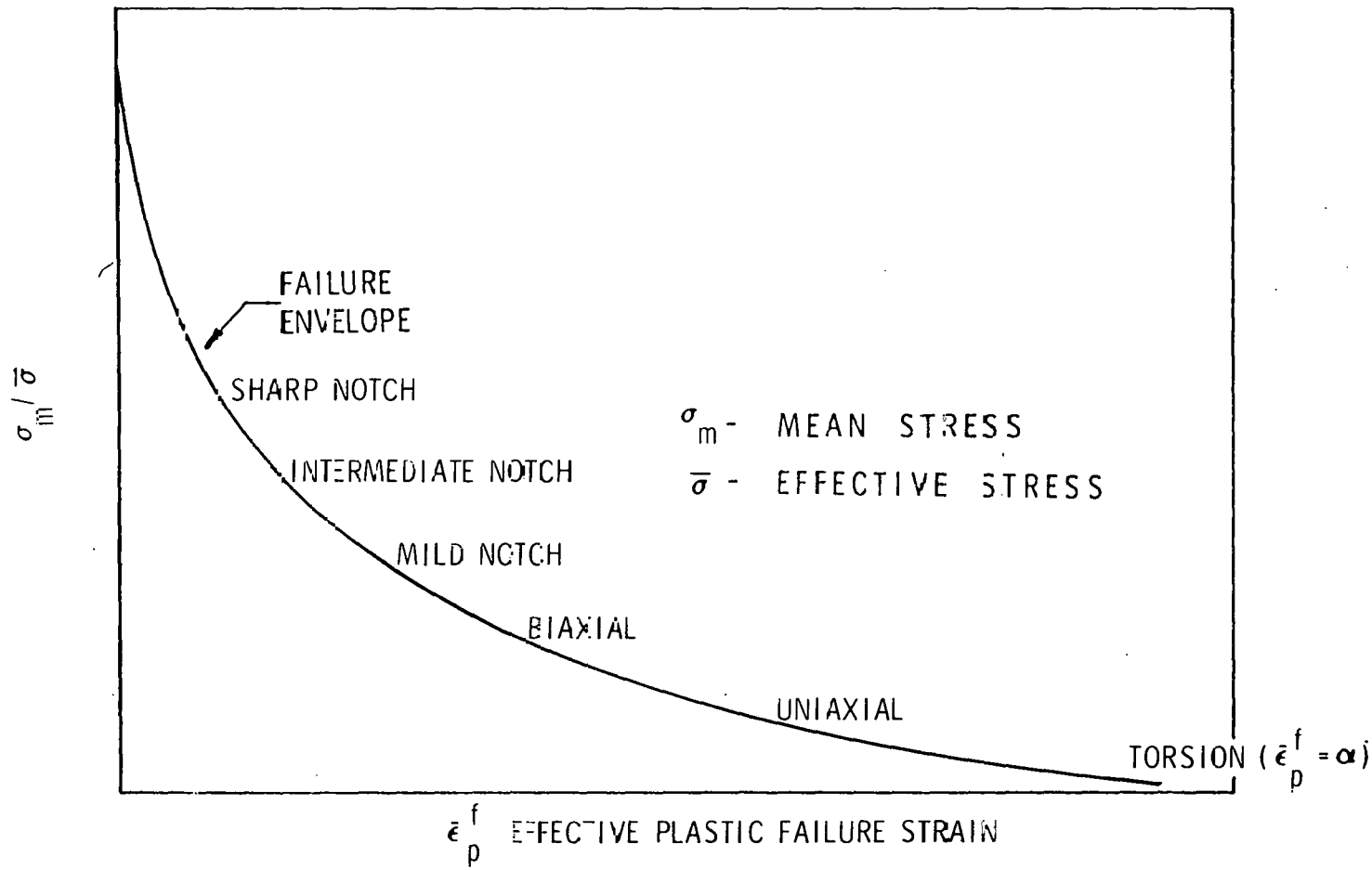

Fig. 1 - Hancock-MacKenzie Model

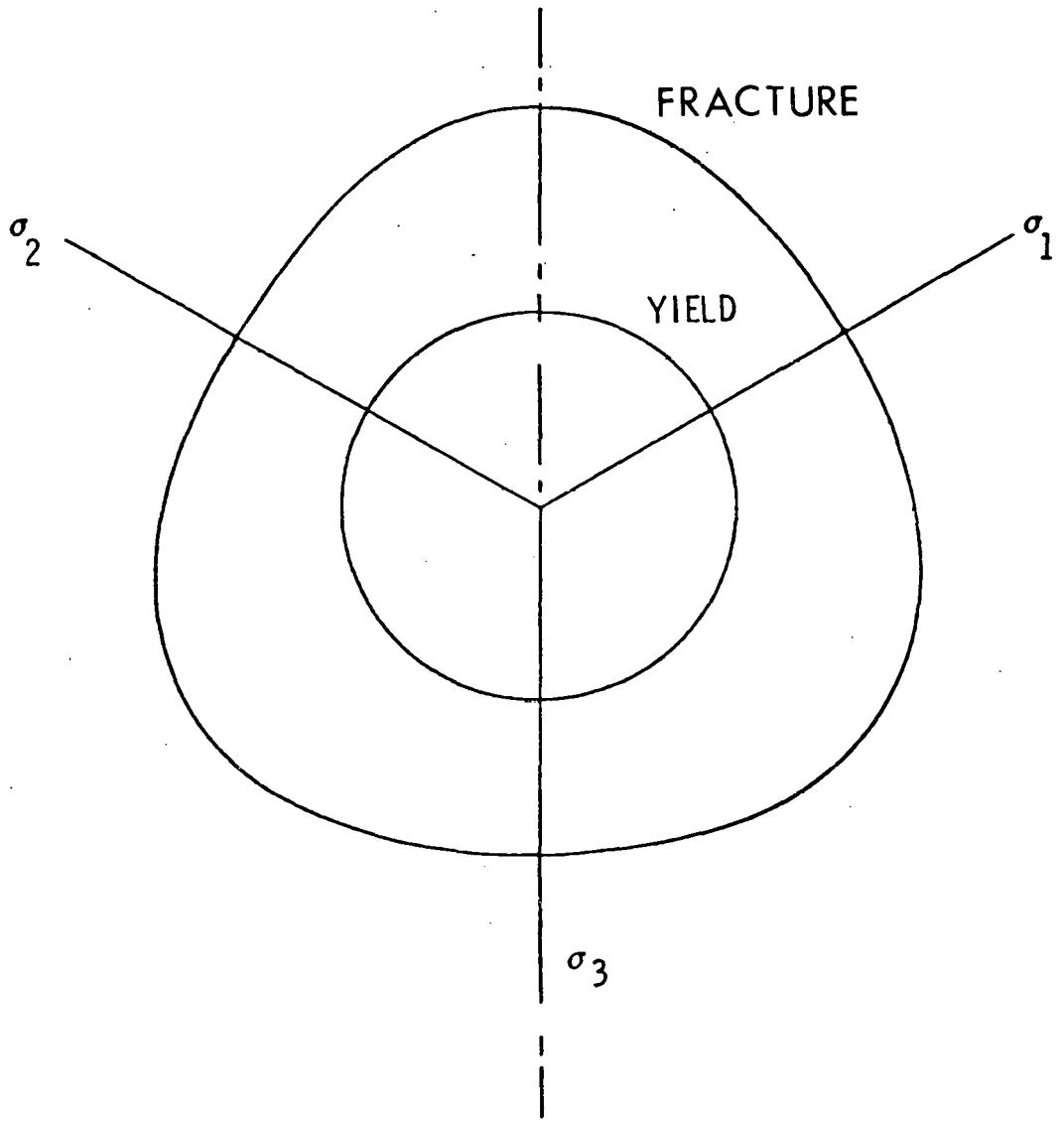

Fig. 2 - Cross Section of Priddy

Model Taken Perpendicular to Hydrostatic Axis

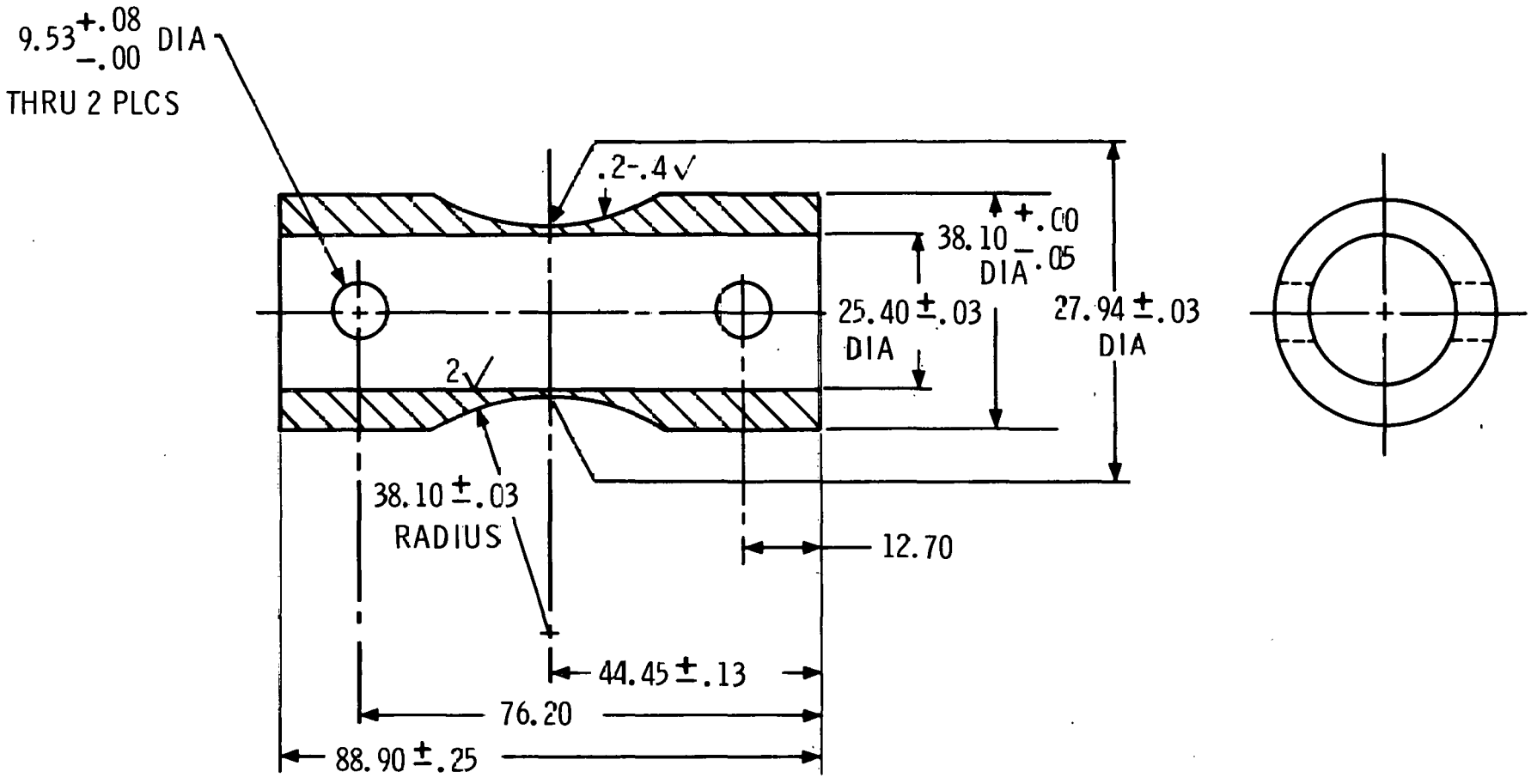

Fig. 3 - Hollow Torsion Specimen

(Dimensions in mm)

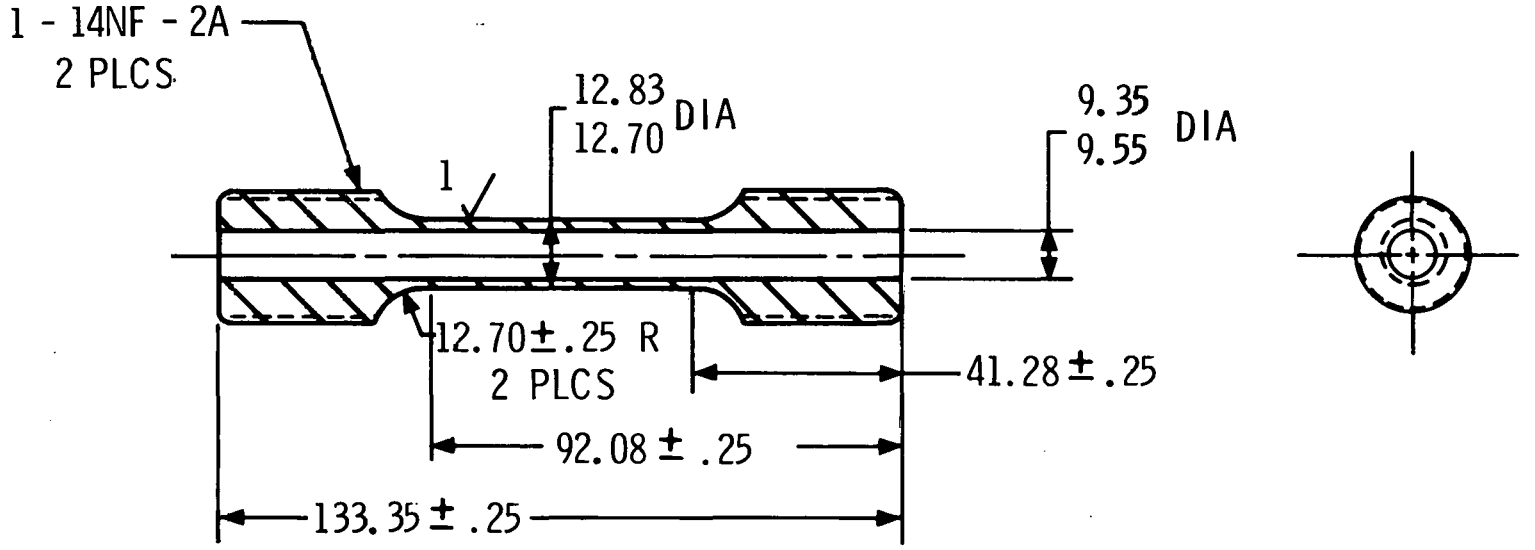

Fig. 4 - Uniaxial Tubular Specimen

(Dimensions in mm)

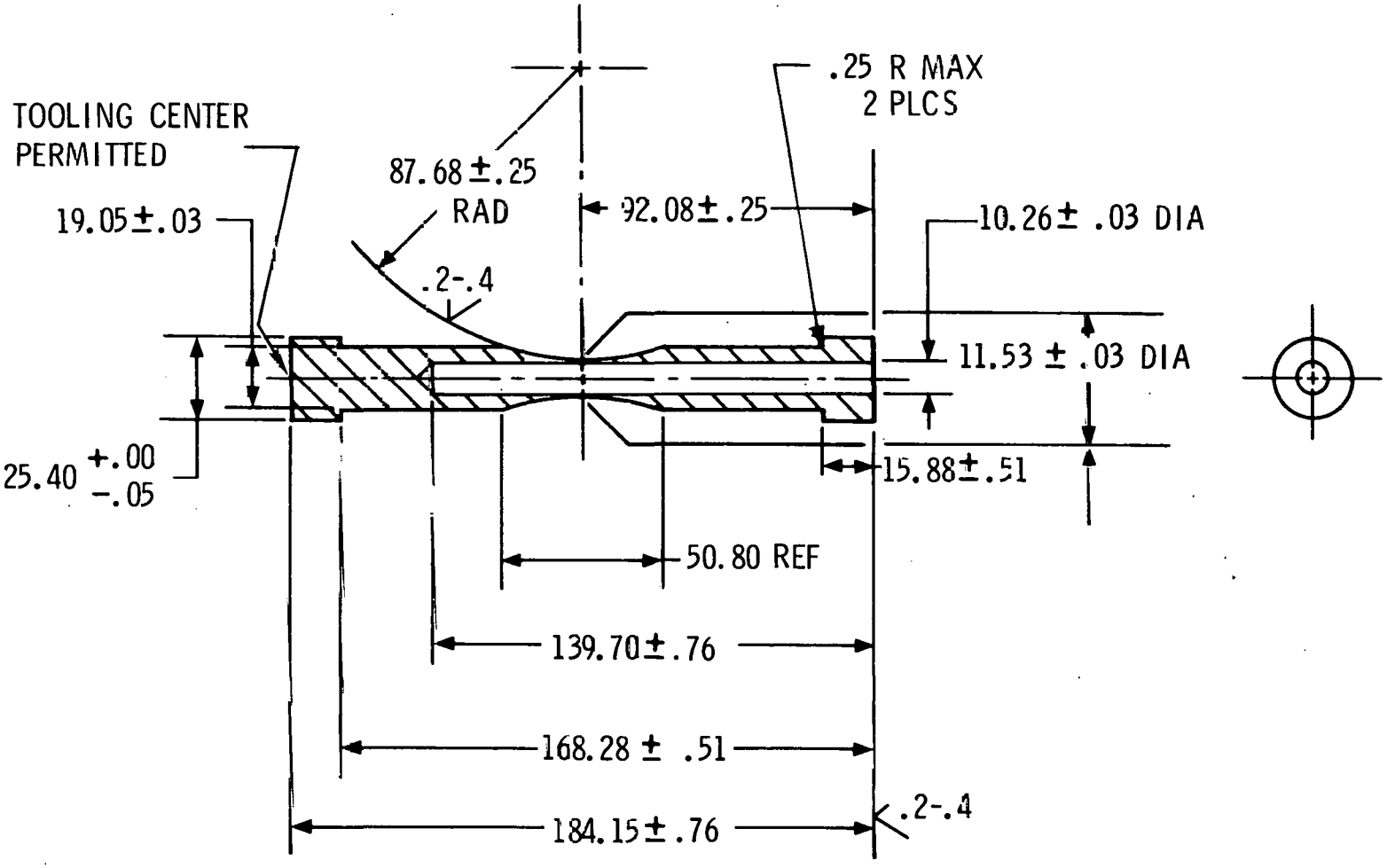

Fig. 5 - Biaxial Tubular Specimen

(Dimensions in mm)

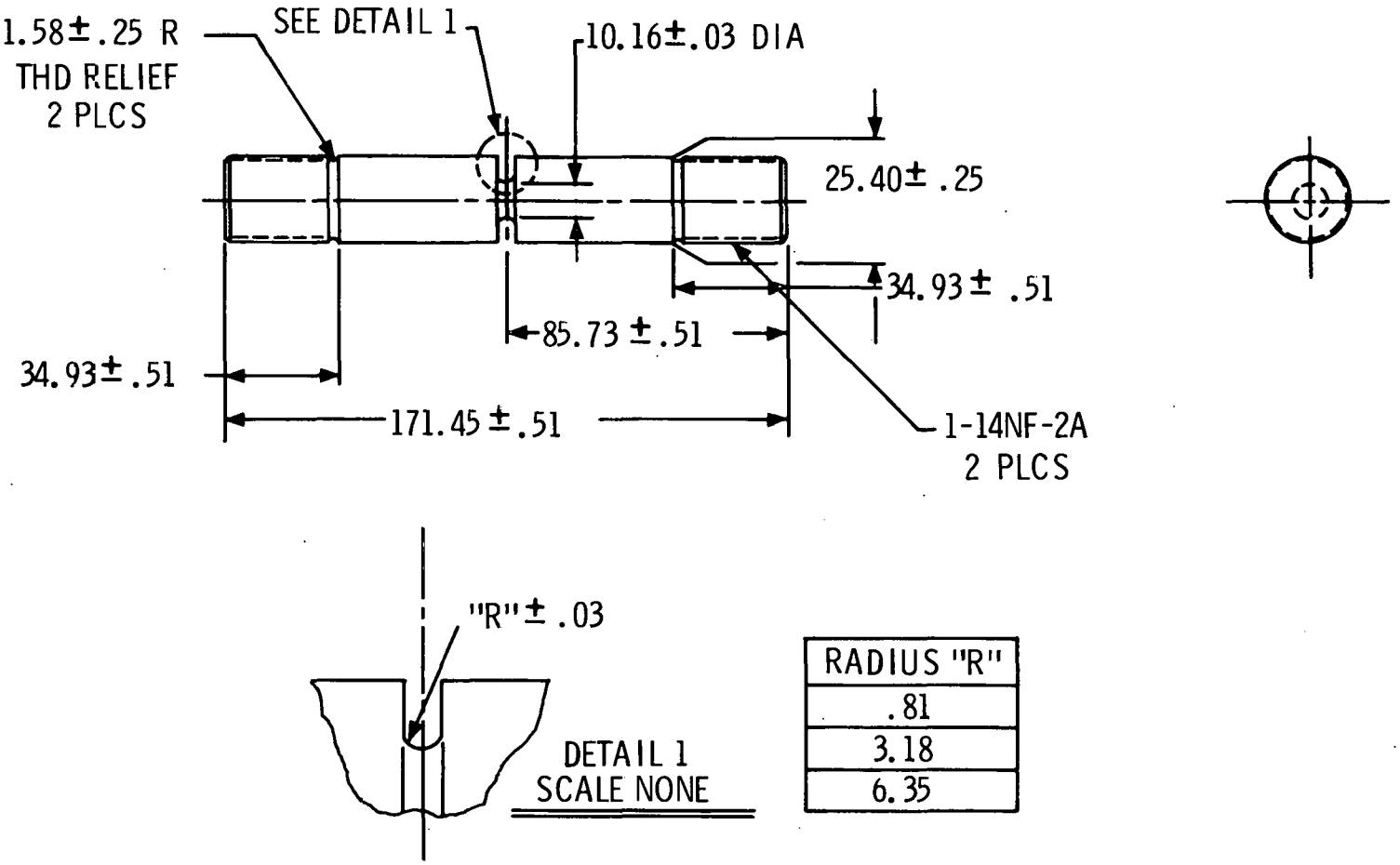

Fig. 6 - Triaxial Notched Round Bar Specimen

(Dimensions in mm)

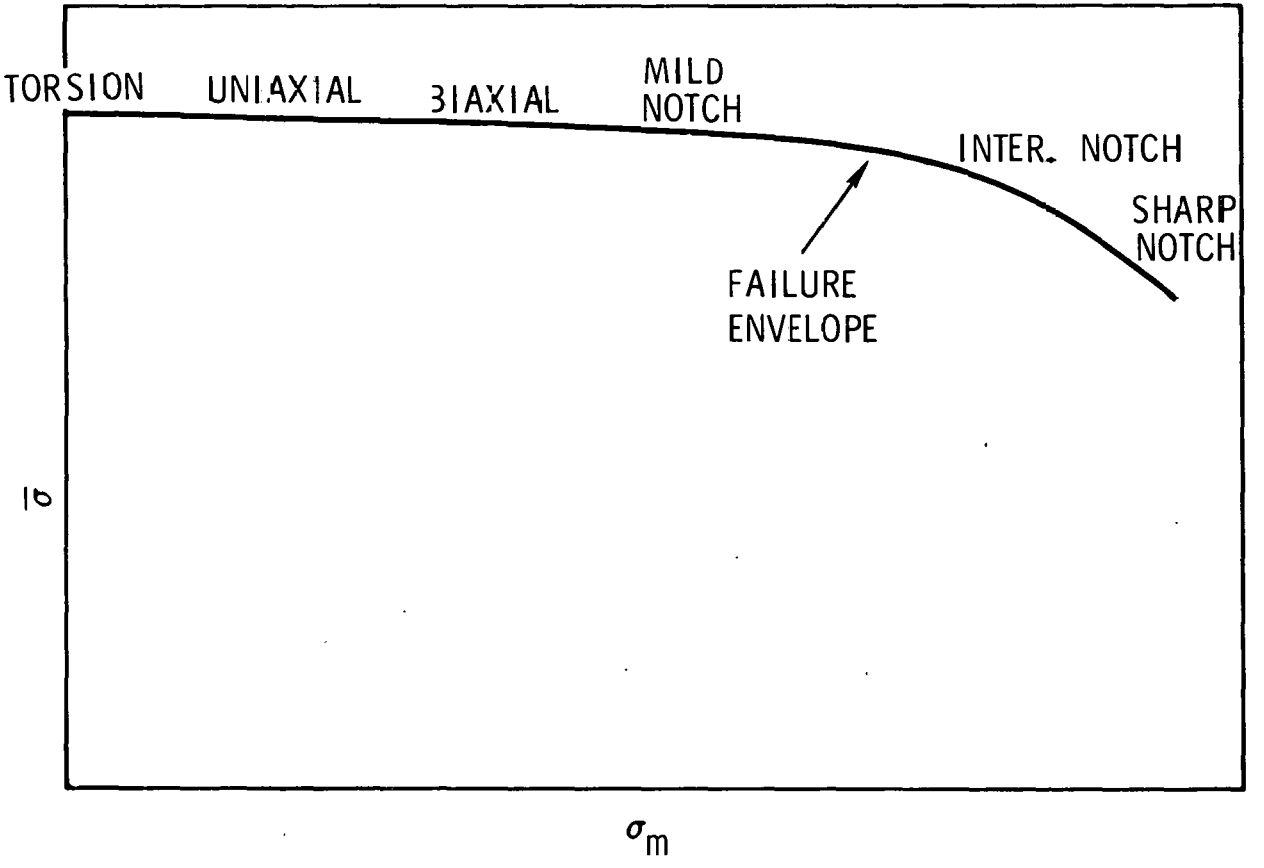

Fig. 7 - Predicted Failure Locus

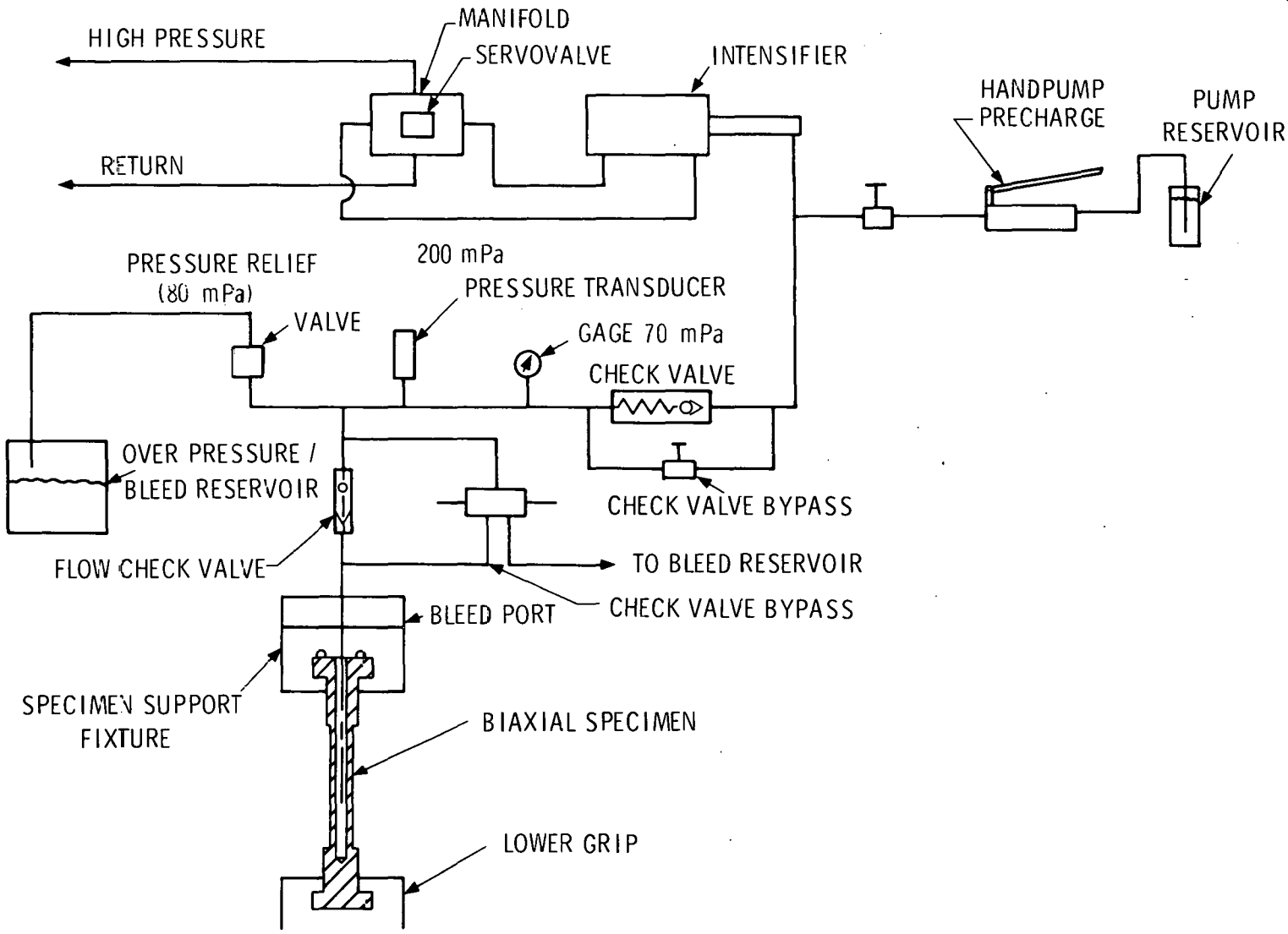

Fig. 8 - Diagram for Pressurization of Biaxial Specimens

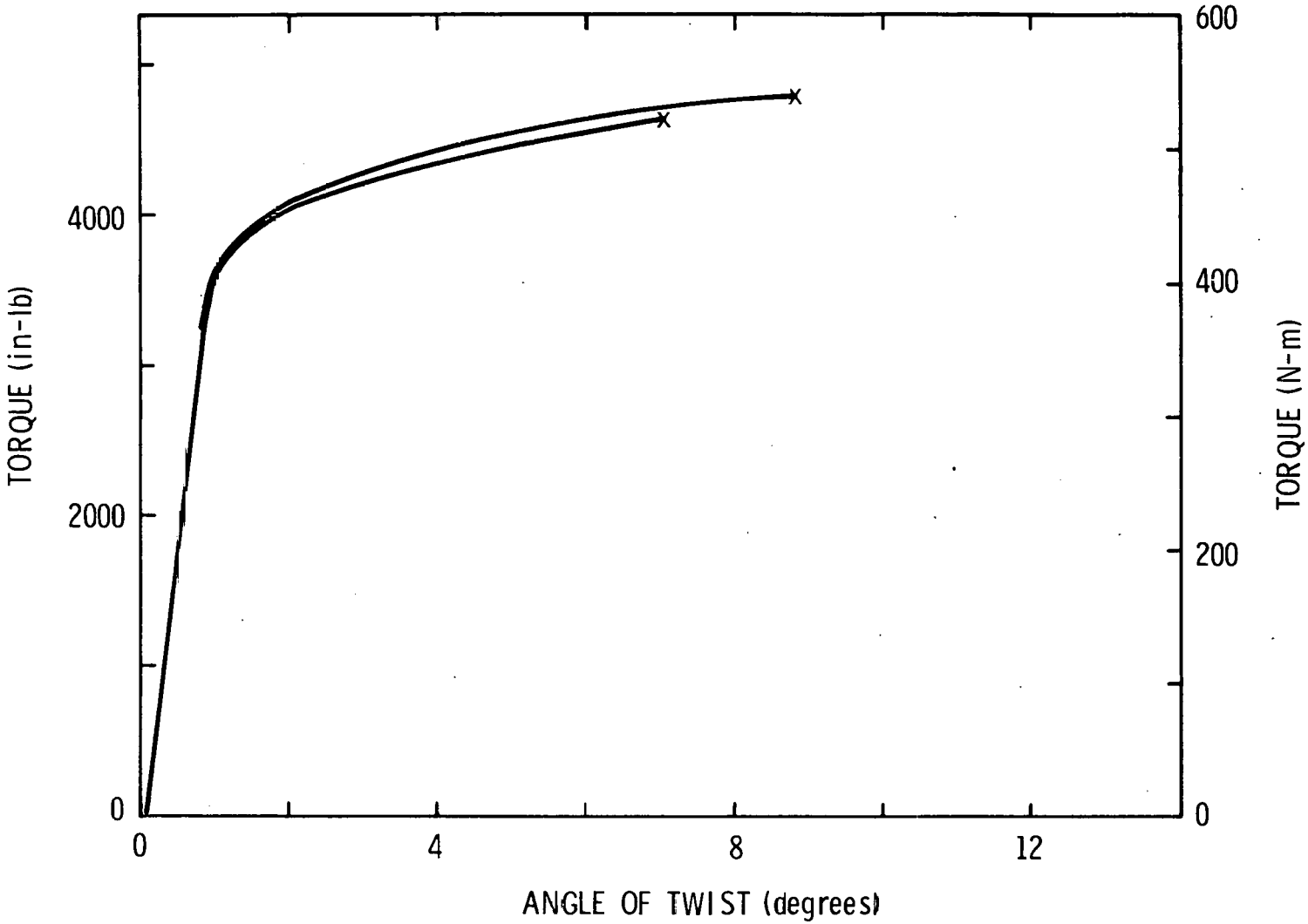

Fig. 9 - Torsion Data

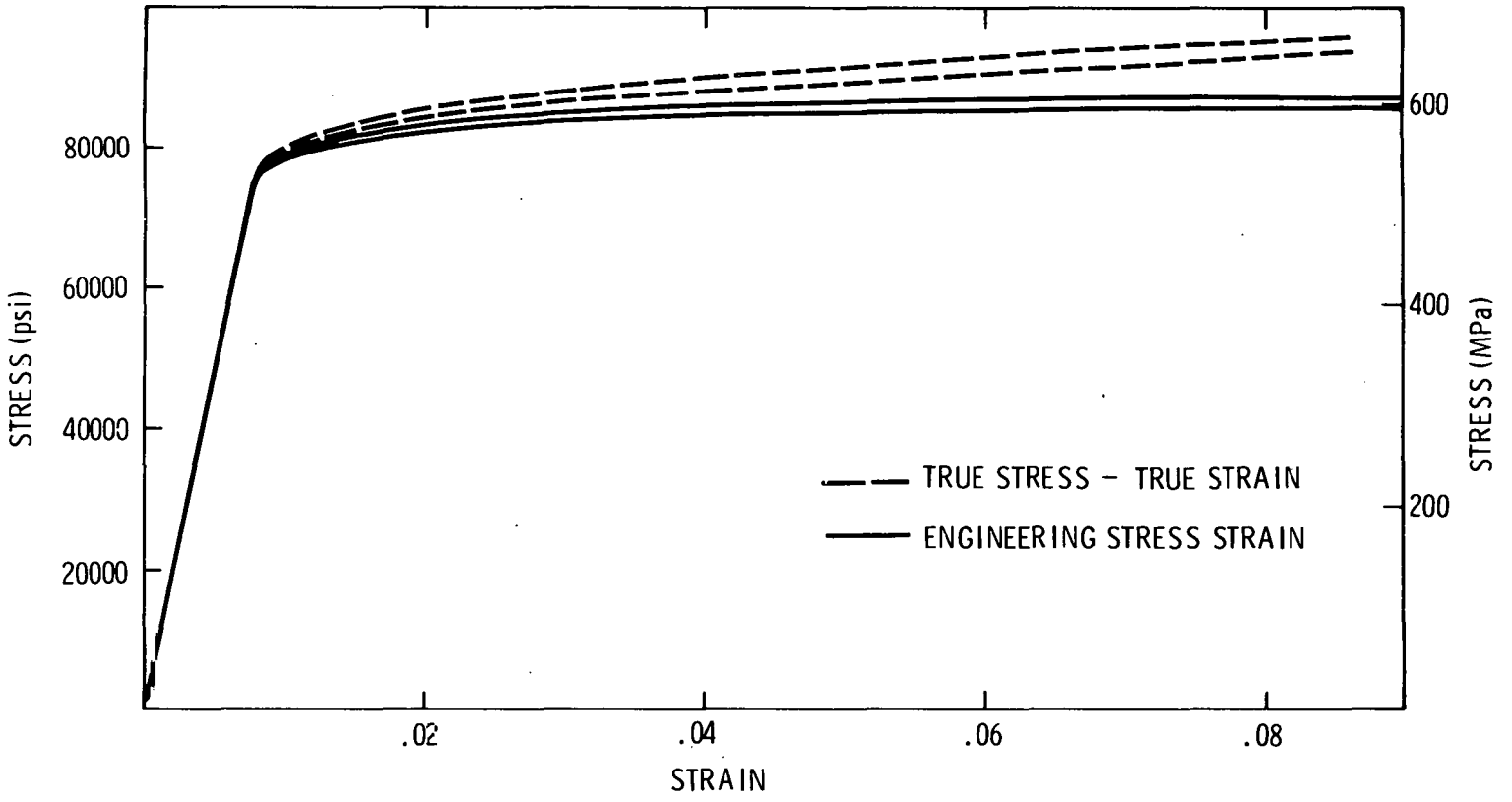

Fig. 10 - Uniaxial Data

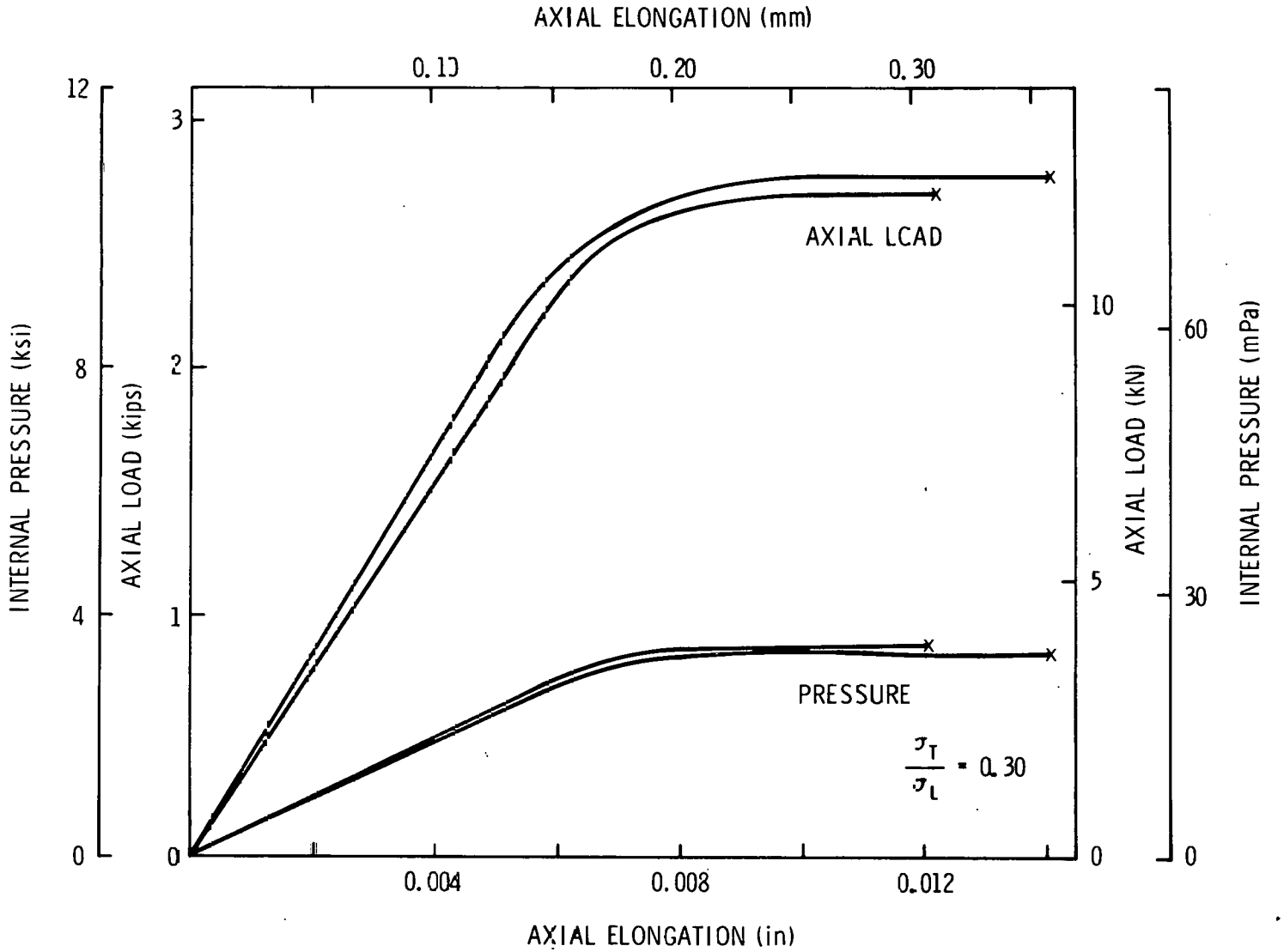

Fig. 11 - Biaxial Data

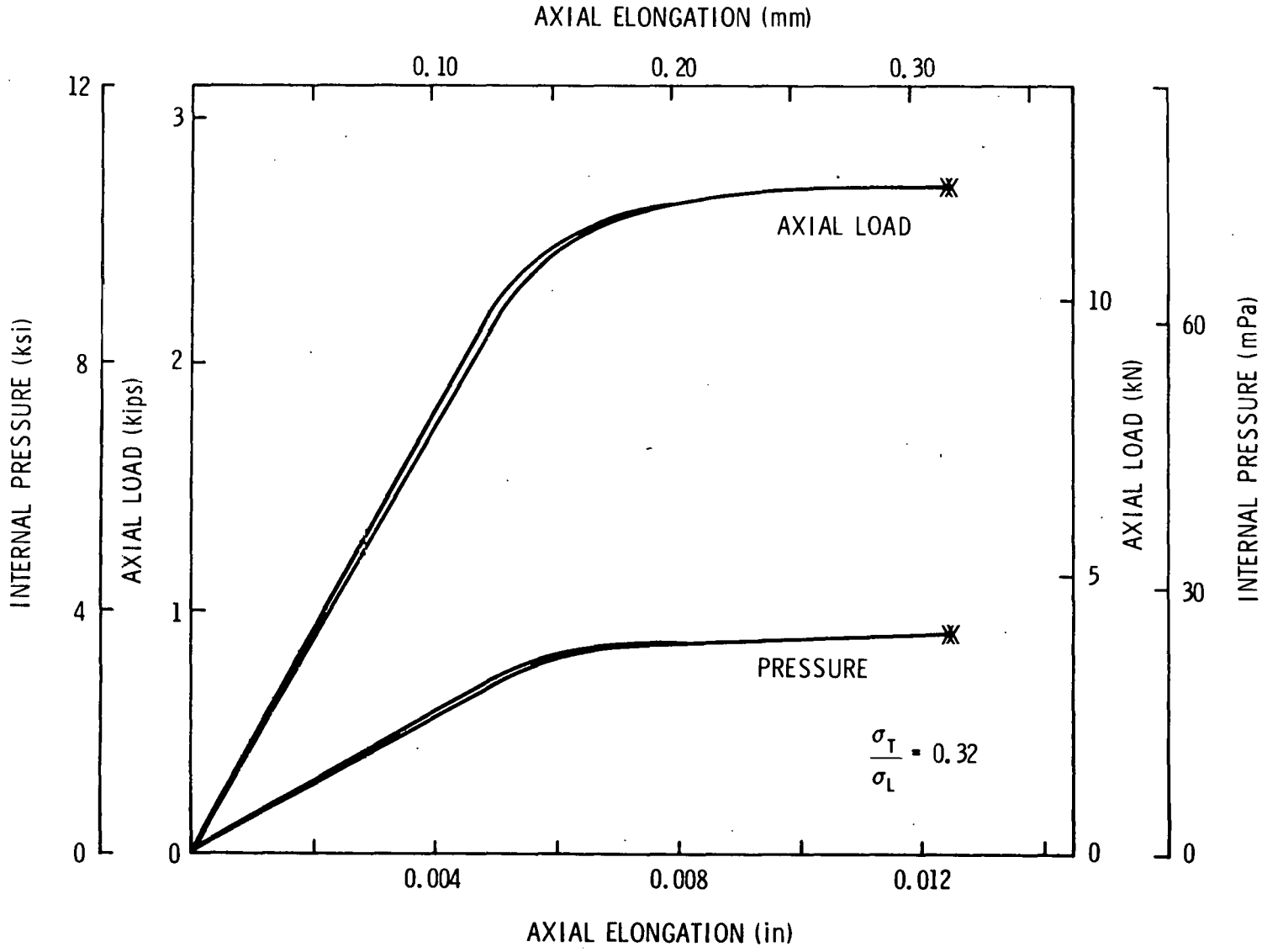

Fig. 12 - Biaxial Data

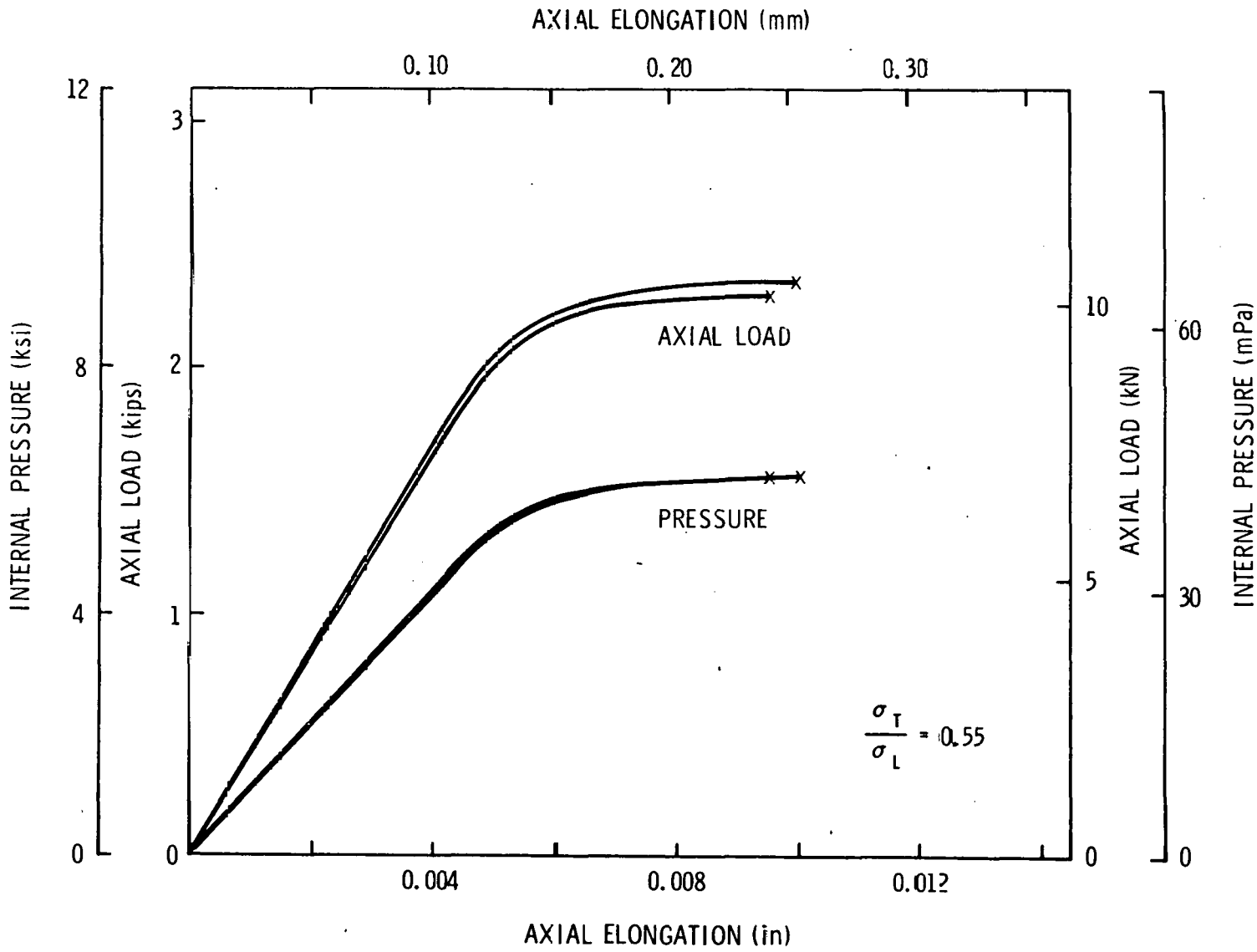

Fig. 13 - Biaxial Data

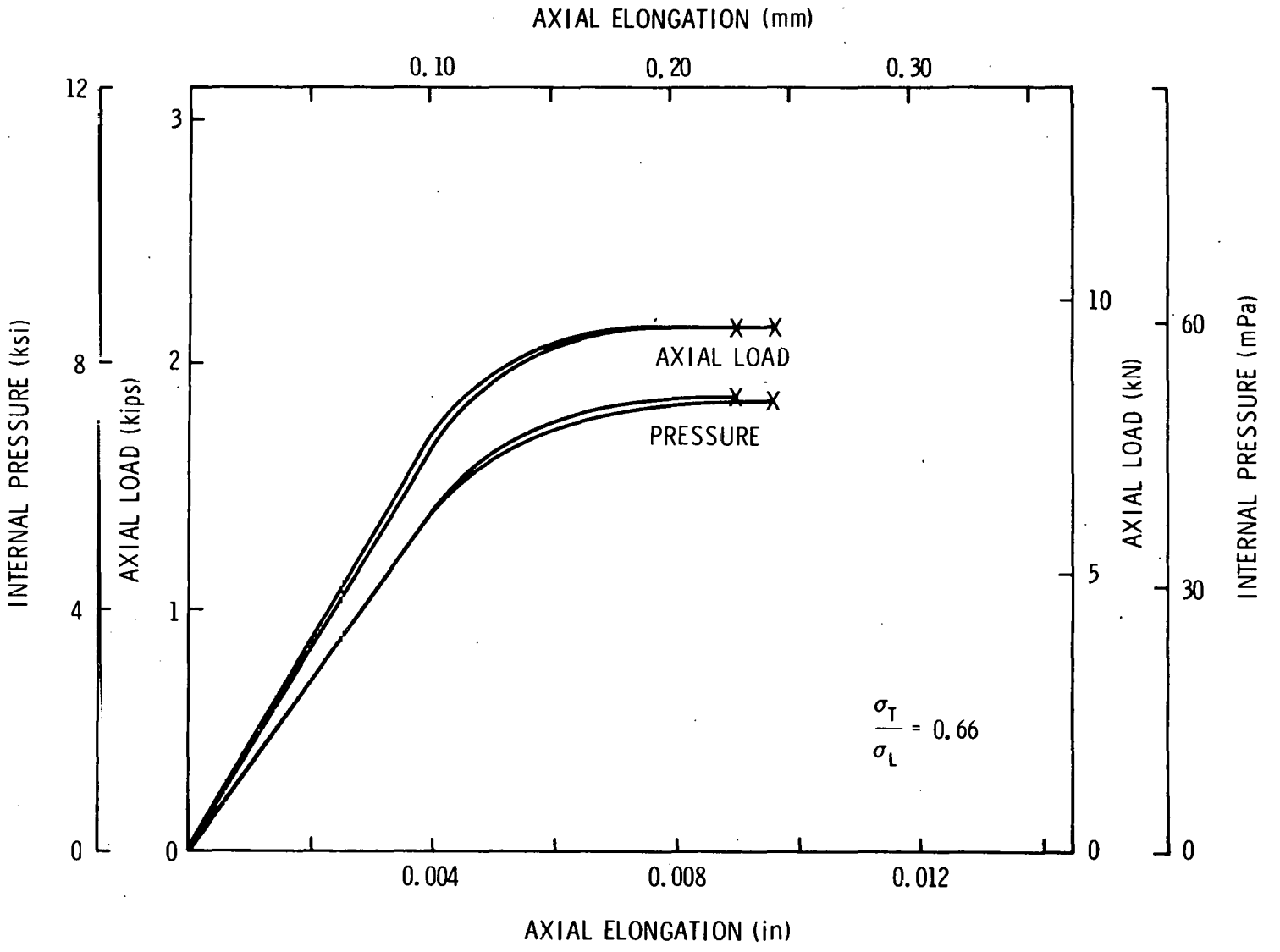

Fig. 14 - Biaxial Data

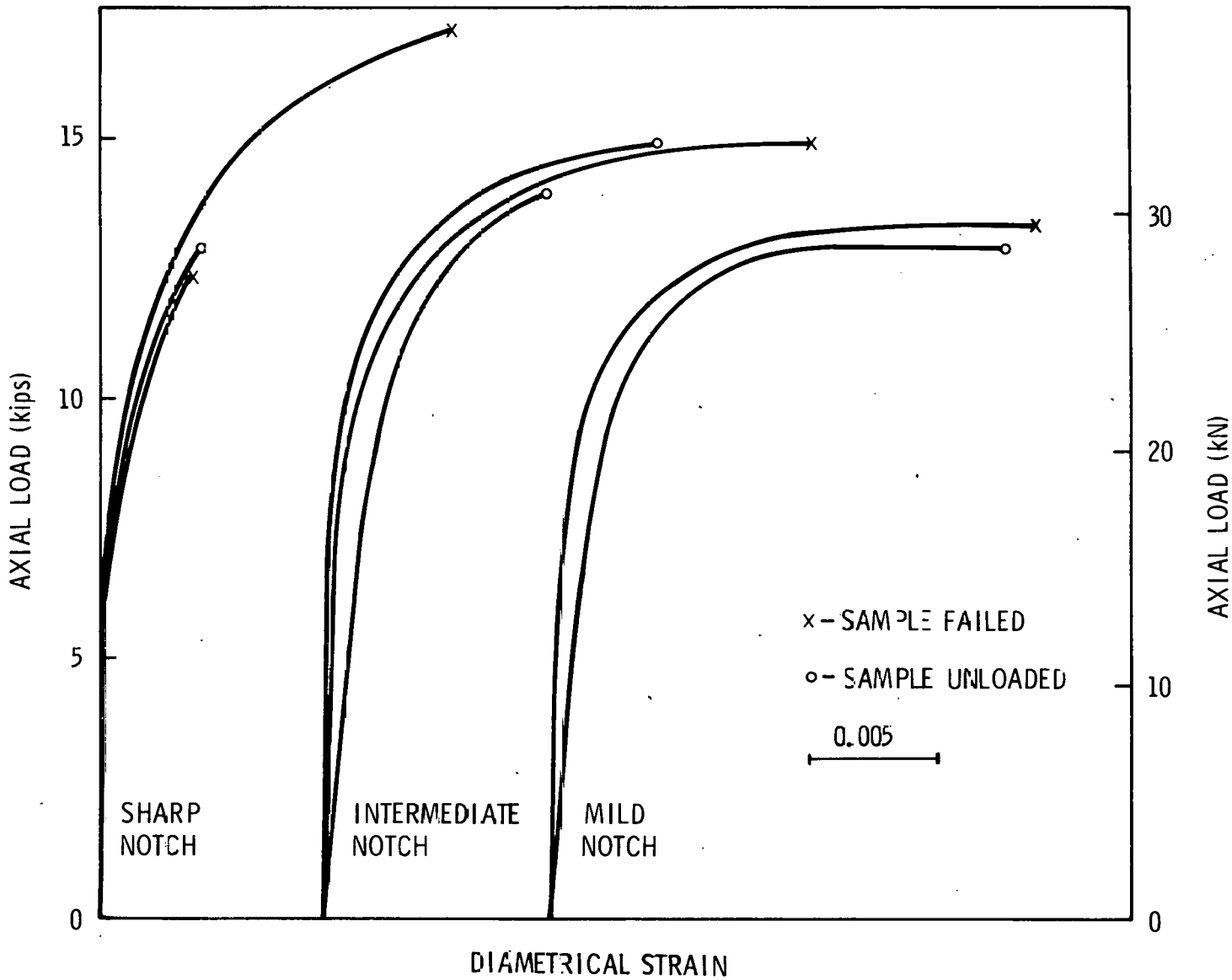

Fig. 15 - Triaxial Data

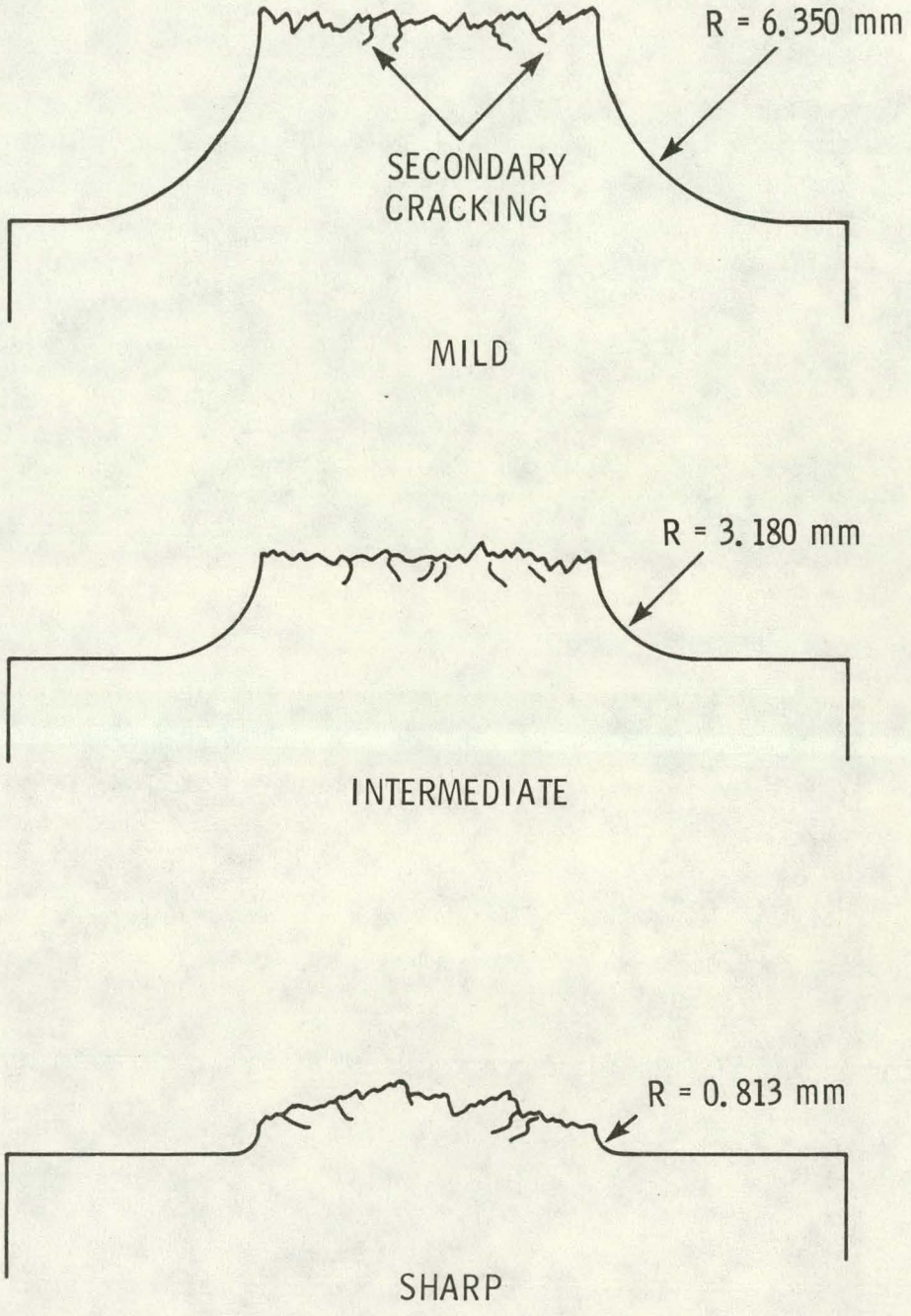

Fig. 16 - Profile of Fractured Notch Round Bar Specimens Showing Secondary Cracking

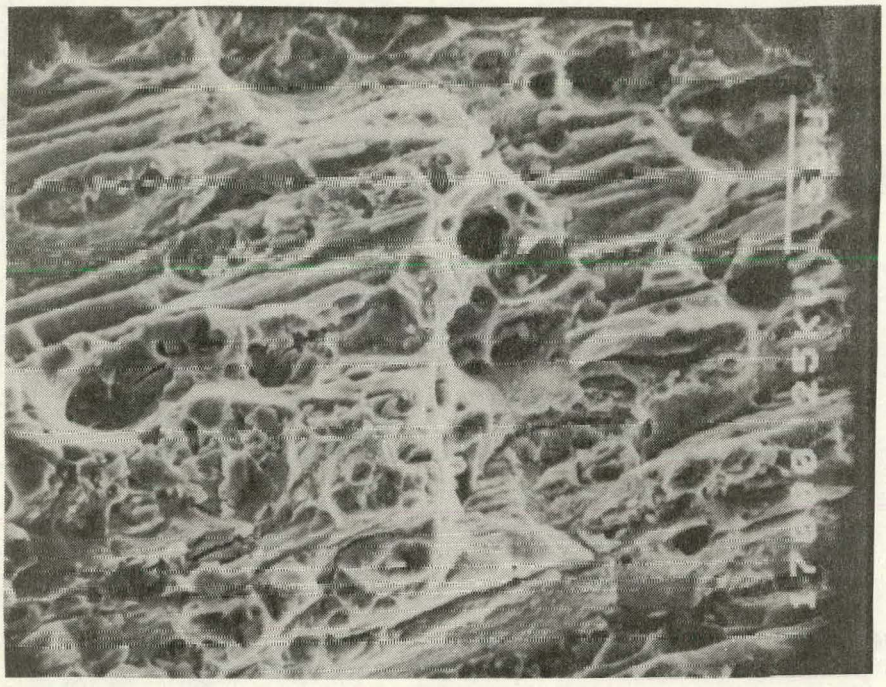

Mild Notch - Center (400X)

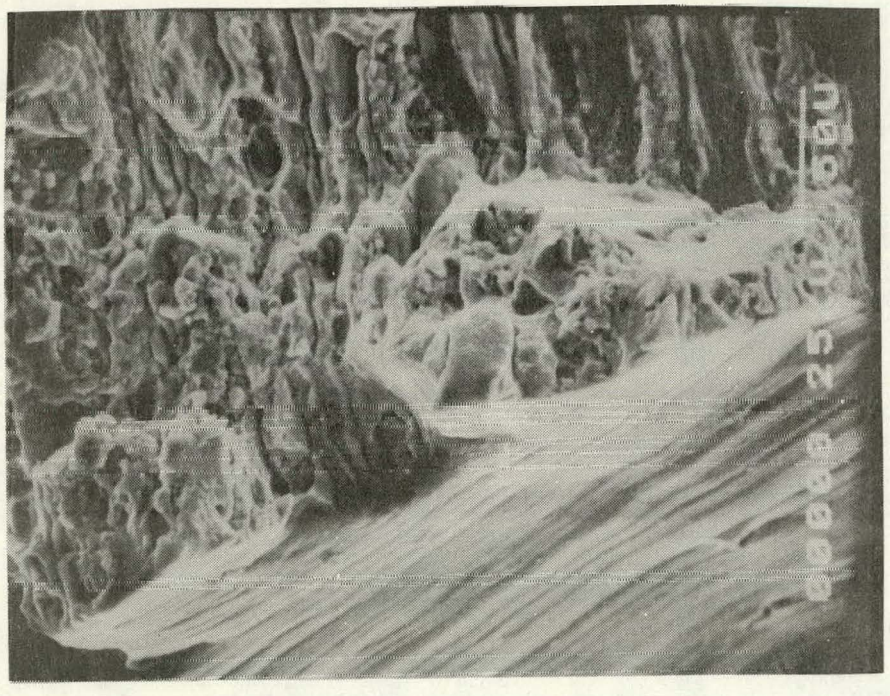

Sharp Notch (400X)

Fig. 17a - SEM Fractograph of
Mild and Sharp Notch

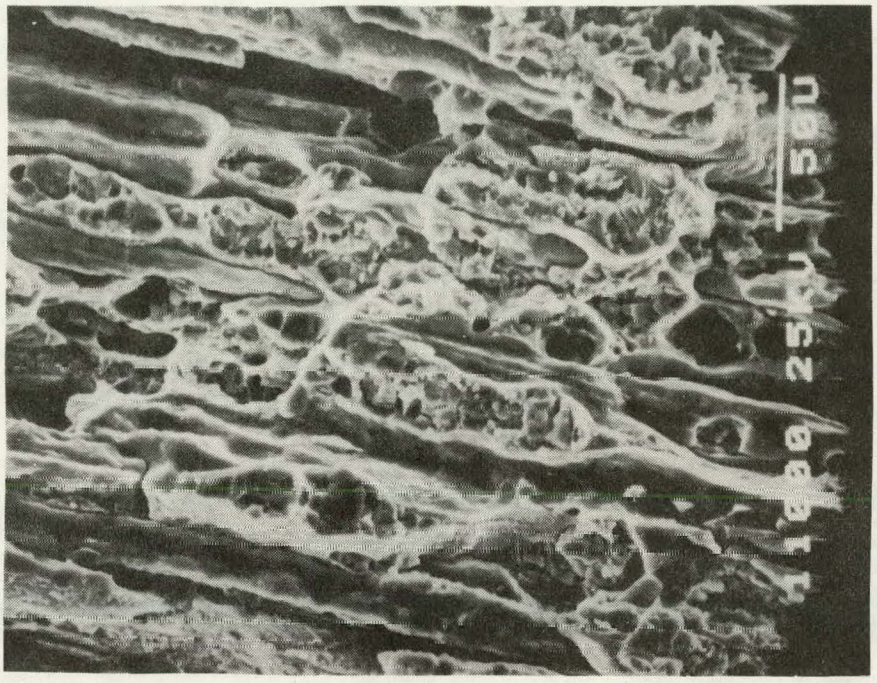

Intermediate Notch (400X)

Fig. 17b - SEM Fractograph of
Intermediate Notch

This Page Intentionally Left Blank.

Distribution:

Peter D. Hilton
A. D. Little, Inc.
Acorn Park
Cambridge, MA 02140

5521 R. D. Krieg
5522 T. G. Priddy (4)
5522 S. E. Benzley (4)
5522 J. T. Black
5523 R. E. Reuter
5524 R. T. Othmer
5531 S. W. Key
5830 M. J. Davis
5832 R. W. Rohde
5833 J. L. Jellison
5834 D. M. Mattox
5835 R. E. Blose
5835 W. B. Jones
5835 C. H. Karnes
5835 H. J. Rack
5835 M. S. Soo Hoo (4)
5835 J. A. Van Den Avyle
5836 J. L. Ledman
5837 R. S. Blewer
8121 B. A. Benedetti
8121 M. L. Callabresi
8122 C. S. Hoyle
8123 W. D. Zinke
8123 M. W. Perra
8123 T. Mamaros
8316 J. C. Swearengen
3141 T. L. Werner (5)
3144 Central Technical File
3151 W. L. Garner (3)
DOE/TIC (25)
(R. P. Campbell, 3172-3)

Org.	Bldg.	Name	Rec'd by *	Org.	Bldg.	Name	Rec'd by